

## Synthesis of superhydrophobic polymer/tungsten (VI) oxide nanocomposite thin films

Sebastian Dixon <sup>1</sup>, Nuruzzaman Noor <sup>2</sup>, Sanjayan Sathasivam <sup>3,4</sup>, Yao Lu <sup>5</sup> and Ivan Parkin <sup>6,\*</sup>

<sup>1</sup> Department of Chemistry, University College London, London, WC1H 0AJ, United Kingdom

<sup>2</sup> Department of Chemistry, University College London, London, WC1H 0AJ, United Kingdom

<sup>3</sup> Department of Chemistry, University College London, London, WC1H 0AJ, United Kingdom

<sup>4</sup> Bio Nano Consulting Ltd., The Gridiron Building, One Pancras Square, London, N1C 4AG, United Kingdom

<sup>5</sup> Department of Chemistry, University College London, London, WC1H 0AJ, United Kingdom

<sup>6</sup> Department of Chemistry, University College London, London, WC1H 0AJ, United Kingdom

\* Corresponding author at: Department of Chemistry, University College London, London, WC1H 0AJ, United Kingdom.  
Tel.: +44.20.76794669. Fax: +44.20.76797463. E-mail address: [ip.parkin@ucl.ac.uk](mailto:ip.parkin@ucl.ac.uk) (I. Parkin).

### ARTICLE INFORMATION



DOI: 10.5155/eurjchem.7.2.139-145.1395

Received: 15 January 2016

Accepted: 06 February 2016

Published online: 30 June 2016

Printed: 30 June 2016

### KEYWORDS

Tungsten  
Thin films  
Nanoparticles  
Materials science  
Hydrophobic effect  
Chemical vapor deposition

### ABSTRACT

A method is presented to enable the preparation of superhydrophobic polymer/tungsten (VI) oxide (WO<sub>3</sub>) nanocomposite coatings on glass substrates. WO<sub>3</sub> nanoparticles were incorporated via the swell-encapsulation-shrink method into superhydrophobic silicone polymer films deposited on glass via aerosol-assisted chemical vapour deposition (AACVD) to produce the novel nanocomposite films. The technique overcomes the limitations of previous methods for nanoparticle incorporation to provide a synthetic route to previously unattainable materials. The nanocomposite films retain the properties of the superhydrophobic polymer while the presence of the nanoparticles is clearly evident. As such, the films have a range of potential applications including high surface area photocatalysis and self-cleaning photochromic or electrochromic coatings. The two-stage synthesis is shown to be flexible and suggests great scope for producing any number of future novel materials. The thin films were characterized using scanning electron microscopy (SEM), energy-dispersive X-ray (EDX) analysis, X-ray photoelectron spectroscopy (XPS), infra-red (FTIR) spectroscopy, X-ray diffractometry (XRD) and water droplet contact angle measurements.

Cite this: *Eur. J. Chem.* **2016**, *7*(2), 139-145

### 1. Introduction

Superhydrophobic surfaces have existed in the natural world for time immemorial, the classic example being the Lotus leaf for which the self-cleaning *Lotus effect* is named [1,2]. In recent years however, biomimetic synthetic superhydrophobic coatings have become a new breed of material which have attracted widespread attention not only for their self-cleaning capability [3], but also more recently on account of their high specific surface area, corrosion resistance, flexibility of application, resistance to bacterial adhesion and relative ease of deposition [4,5]. In particular, the deposition of polymeric superhydrophobic films has opened up the way for a new generation of smart composite materials which combine the benefits of both superhydrophobic and nanocomposite factors by incorporation of functional nanoparticles into the polymer's microstructure. Such superhydrophobic nanocomposite materials have already been prepared incorporating titania, Au@SiO<sub>2</sub> (yolk-and-shell), iron (II/III) oxide, cobalt oxide and nickel nanoparticles [6]. In the previous work by Crick *et al.*, these

nanocomposite coatings comprising both the superhydrophobic polymer material and the nanoparticles were deposited on glass in a single step via aerosol-assisted chemical vapour deposition [6], which has attracted attention as a deposition technique on account of its ability to deposit non-volatile material as a uniform film on a substrate [3]. However, limitations to the technique were encountered when attempting the 'one-pot' deposition of the polymer with some species of metal-oxide nanoparticles, or with uncoated gold nanoparticles. Some species of metal oxide nanoparticles such as cobalt (II) oxide would agglomerate within the precursor vessel, inhibiting their uptake by the aerosol droplet and ultimately resulting in polymer deposition but with a lack of nanoparticle incorporation. On the other hand, gold or nickel nanoparticles would interfere with the noble metal-based catalysis of the polymerisation process, resulting in little polymer deposition [6].

Other previous, well-established methods for achieving nanoparticle incorporation into a polymer film include supercritical fluid deposition (SFD), in which nanoparticles are synthesised in-situ by a wet chemical reduction of a metal salt

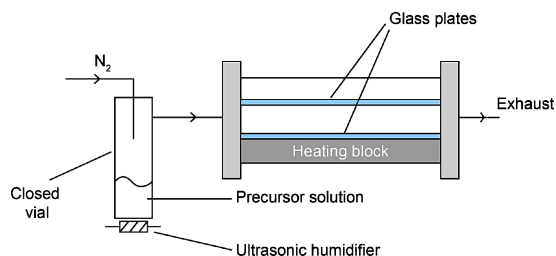


**Figure 1.** Schematic of benchtop AACVD apparatus used in deposition of superhydrophobic polymer films.

within the polymer matrix [7], and the 'casting' method, in which the matrix is polymerised around the nanoparticles [8]. However, both inherently require synthesis of one component within or around the other, which naturally affords limited control over polymer dispersity and morphology, and nanoparticle size and/or crystal phase. In the particular case of superhydrophobic films, due to the requirement that the polymer should have a developed surface microstructure, it may be easier to first create a superhydrophobic polymer film, then to incorporate the nanoparticles as a post-deposition step. The present work demonstrates this as a successful and viable alternative via the swell-encapsulation method [9] for incorporation of nanoparticles into a polymer.

Tungsten (VI) oxide in particular has attracted widespread interest in the development of climate-adaptive glass coatings on account of its photochromism, a surface phenomenon that has demonstrated particular promise in recent years [10-12]. The transparency of such materials to certain wavelengths varies depending on the intensity of light incident on the surface due to photoinduced changes in local chemistry. Since the intensity of solar ultraviolet photons incident on a given surface is dependent on the time of day or year, the photochromic effect demonstrates promise for improving the energy efficiency of buildings by automatically insulating or transmitting infrared energy as required. As such, it is hoped that this technology might lead us to reduced reliance on wasteful use of heating and cooling technologies, helping us to operate greener industry and households.

Tungsten (VI) oxide has a number of temperature-dependent crystal phase transitions [13], which vary the band gap and number of surface oxygen vacancies available [10]. Such properties are crucial to the functionality of a photochromic nanocrystal. Therefore, the ability of a nanocomposite containing tungsten (VI) oxide to behave as a photochromic material is highly dependent on the temperatures involved in its processing. Swell-encapsulation of nanoparticles can occur at room temperature, unlike the 'one-pot' AACVD incorporation, so the  $\text{WO}_3$  nanocrystals are at no risk of losing photochromic capacity on account of high-temperature treatment and can be tuned prior to the incorporation. Furthermore, since the photochromic effect arises as a result of surface exchange with the atmosphere, the high specific surface area of tungsten (VI) oxide nanoparticles combined with that of a superhydrophobic polymer matrix presents an opportunity to create a highly efficient, photochromic, self-cleaning coating. The present work demonstrates a synthetic route to previously unattainable superhydrophobic tungsten (VI) oxide/polymer nanocomposite materials, while its ease of application and flexibility leads the way for potentially many more materials to come.

## 2. Experimental

### 2.1. Characterization

Scanning Electron Microscopy and Energy Dispersive X-ray spectroscopy were carried out on a JEOL JSM-6301F Field Emission SEM at an accelerating voltage of 5 kV, with an attached Oxford Instruments INCA Energy EDXA system. Raman spectroscopy was performed on a Renishaw inVia Raman microscope with a 785 nm red laser, measuring in the frequency range 50-1200  $\text{cm}^{-1}$ . Attenuated Total Reflectance Fourier-Transform Infra-Red spectroscopy was carried out on a Bruker Platinum ATR FT-IR instrument, measuring in the frequency range 400-4000  $\text{cm}^{-1}$ . Thin film X-Ray Diffraction was carried out on a Bruker D8 diffractometer with parallel beam and grazing incidence angle optics equipped with  $\text{Cu K}\alpha_{1+2}$  source powered at 40 kV, 40 mA and coupled with a LynxEye silicon strip detector. Measurements were taken in the range  $2\theta = 10-66^\circ$ , with the X-ray tube at  $1^\circ$ , and detector steps of  $0.05^\circ$  with 1 s per step. Water droplet contact angles were measured using an FTA-1000 B-class drop shape instrument, dispensing 5  $\mu\text{L}$  water droplets and measuring droplet shapes with Laplace-Young fitting.

### 2.2. Aerosol-assisted chemical vapour deposition of superhydrophobic film

#### 2.2.1. Apparatus

The AACVD apparatus was arranged as in Figure 1, where a solution of polymer precursor in the flask is nebulised into an aerosol by an ultrasonic humidifier, whereupon an inert carrier gas ( $\text{N}_2$ ) passes through the generated aerosol at a set flow rate to transport the aerosol particles to the heated reaction chamber. The aerosol enters the chamber between a pair of parallel barrier glass plates separated by a known height above and below the injection point, whereupon the aerosol particles containing the polymer precursor will cure to deposit on the top plate. The carrier gas continues out of the exhaust at the far end of the reaction chamber. The use of barrier glass as a substrate is common practice in the preparation of thin films; the silica layer (barrier) at the surface of the float glass prevents ion exchange with, and therefore contamination of, the thin film.

#### 2.2.2. Procedure

In a typical experiment (as outlined in Figure 2), the Sylgard-184 two-part silicone elastomer and curing agent, purchased from Univar Specialty Consumables, were combined in a 10:1 ratio (0.5 g base material, 0.05 g curing agent) and dissolved in chloroform (~50 mL) with stirring. The flask containing the mixture was then connected to the AACVD apparatus for immediate deposition, in order to minimise premature curing. Having heated the AACVD reactor chamber to  $390^\circ\text{C}$ , a Johnson Matthey Liquifog ultrasonic humidifier was used to generate an aerosol from the precursor solution. The precursor was added in two halves to the flask, through a funnel under positive pressure of nitrogen gas, in order to reduce the difficulty of generating an aerosol from

this relatively large volume of liquid. Nitrogen gas was passed through the precursor flask at a flow rate of 1.0 L/min.

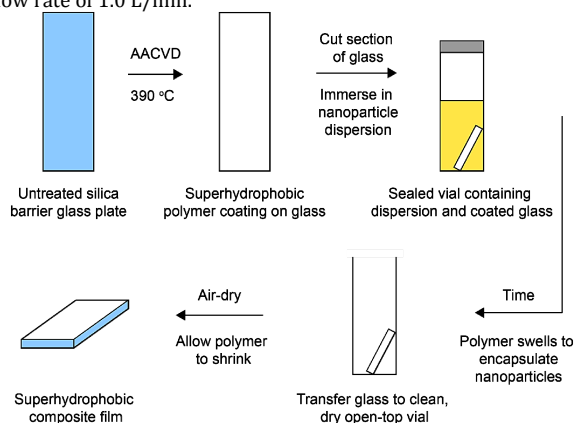


Figure 2. Schematic of procedure for synthesizing superhydrophobic nanocomposite thin films.

The silica barrier glass plates (each  $145 \times 45 \times 5$  mm) were separated by a distance of 8 mm within the chamber. The bottom of the two plates rested upon a heated carbon block, whose temperature was monitored and regulated by a thermocouple. The top plate, as measured manually with a handheld thermocouple, reached a maximum temperature of approximately  $310$  °C. The temperature gradient between the two plates leads to the thermophoresis phenomenon, with deposition of cured elastomer microparticles occurring exclusively on the top plate. The deposition process was continued until all of the precursor solution had been converted to aerosol (approximately 45 min). At this point, the heating element was turned off and the reaction chamber allowed to cool, containing the plates, for approximately 30 min to room temperature under the flow of nitrogen. The plates were then removed from the reactor chamber and handled in air.

### 2.3. Functionalization of tungsten (VI) oxide nanoparticles

In a typical experiment, yellow tungsten (VI) oxide nanopowder (1.0 g, 4.3 mmol, < 100 nm), as purchased from Aldrich, was added to oleic acid (40 mL, 125 mmol) and a catalytic amount of triethylamine (1.0 mL, 7.2 mmol), both purchased from Sigma-Aldrich, with vigorous stirring at  $70$  °C for 96 h. The resulting yellow oleate-capped tungsten oxide nanoparticles were precipitated by addition of ethanol (~100 mL), followed by centrifugation at 4500 rpm for 10 min. The colourless supernatant was decanted and the yellow nanoparticles washed with ethanol ( $2 \times 80$  mL) then dispersed in chloroform (150 mL).

### 2.4. Swell encapsulation of nanoparticles into elastomer film

The superhydrophobic elastomer film was prepared on glass as per the AACVD method detailed above. An excess of oleic acid-functionalized  $\text{WO}_3$  nanoparticles (~0.2 g) is dispersed in chloroform (~10 mL) to form a milky-yellow saturated dispersion (the "100% saturated" dispersion). Then, in a typical swell-encapsulation process, smaller sections cut from the glass ( $20 \times 10 \times 5$  mm) were totally immersed in the nanoparticle dispersion. For lower-concentration encapsulation, the saturated dispersion was decanted (such that the residual nanoparticles in the bottom of the flask were not transferred) and diluted to 25% with additional chloroform. An additional cut section of the polymer-coated glass was allowed to swell in pure chloroform as a control. The samples

were allowed to soak in sealed vessels in a dark cupboard for 2 h. After this period, the nanoparticle dispersion was drained and the glass sample transferred to a clean and dry open-top vial and allowed to air-dry overnight in a dark cupboard to allow the polymer film to shrink, before being rinsed in chloroform then distilled water to dislodge any loose material.

## 3. Results and discussion

### 3.1. Nanoparticle incorporation: preliminary results from 'one-pot' AACVD

Initially, incorporation of tungsten (VI) oxide nanoparticles into a superhydrophobic polymer film was attempted in a 'one-pot' deposition by AACVD, as per the literature method [6]. Tungsten (VI) oxide nanopowder was functionalised with oleic acid in order to render it dispersible in the commercial polymer precursor (Sylgard-184) solution. The nanopowder formed a milky yellow dispersion in the solvent, and a good, cloudy aerosol was formed over the humidifier. However, XRD, EDX and XPS analysis confirmed that no  $\text{WO}_3$  or W was present in the resultant superhydrophobic polymer film, with very little, if any, nanoparticle material therefore having been transported across into the reactor; the overwhelming majority of nanopowder would be left behind in the precursor flask, while the polymer precursor would still transport into the reactor without issue to cure and yield a superhydrophobic film. It is evident that the difficulty encountered here is similar to that in the reported work [6], that agglomeration of the nanoparticles disfavoured uptake by the aerosol droplet, as can be observed in the SEM image of agglomerated  $\text{WO}_3$  nanoparticles in a dip-coated Sylgard-184/ $\text{WO}_3$ -oleate film (Figure 3). Such agglomerates were probably too large or cumbersome for uptake in an aerosol droplet. Thus, these results naturally prompted and supported pursuit of the alternative incorporation method: swell-encapsulation.

### 3.2. Swell testing

A solid segment of the cured Sylgard-184 elastomer, produced for the sake of demonstrating the swelling phenomenon, grew significantly in size from  $18 \times 14$  mm to  $22 \times 18$  mm (swelling ratio = 1.3) upon swelling for 2 h in pure chloroform, returning to its original size upon air-drying overnight. A similar experiment in toluene demonstrated swelling of a polymer segment from  $14 \times 8$  mm to  $19 \times 12$  mm (swelling ratio = 1.4) over a 24 h swelling period. Experiments using more 'hydrophilic' solvents such as methanol and

acetone, however, exhibited very little visible swelling of the polymer. These observations were consistent with those of

previous authors, [14] who had a similar outcome from using these solvents to swell polydimethylsiloxane (swelling ratios

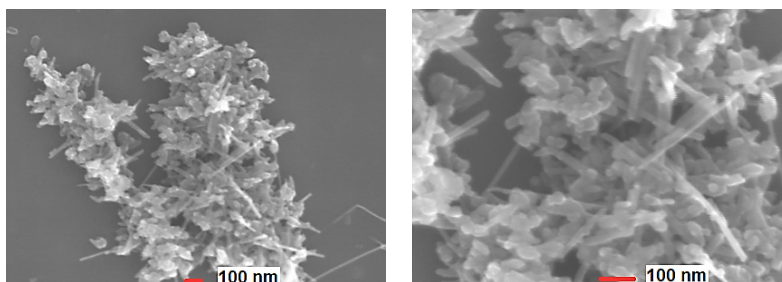


**Figure 3.** SEM images of  $\text{WO}_3$ -oleate nanoparticle agglomerates observed in a dip-coated Sylgard-184/ $\text{WO}_3$ -oleate film on a glass microscope slide, at 43,000 $\times$  (left) and 95,000 $\times$  (right) magnification. Within the clusters, nanoparticles and nanoneedles on the order of approximately 50 nm and 300 nm respectively can be observed.

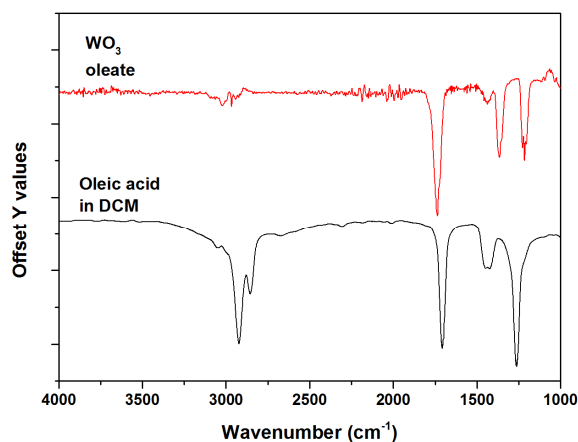


**Figure 4.** Attenuated total reflectance (ATR) FTIR spectrum of oleic acid-functionalised  $\text{WO}_3$  nanoparticles (upper), as compared with that of the oleic acid in dichloromethane (lower).

of 1.39, 1.31, 1.02 and 1.06 for chloroform, toluene, methanol and acetone respectively), which is chemically similar to the commercial Sylgard-184 used here. It was therefore expected that nanoparticle dispersions in chloroform or toluene could diffuse into the polymer matrix much more effectively than methanol or acetone dispersions.

It was also found that chloroform would partially dissolve the superhydrophobic polymer coatings when these were immersed for 24 h. For this reason, the swelling time for chloroform dispersions was set to 2 h, which was found to be sufficient time for the encapsulation of the  $\text{WO}_3$  into the polymer film without degradation of its superhydrophobic properties. A shorter swelling time was also favourable from the point of view of dispersion stability, with the  $\text{WO}_3$  dispersion in chloroform still mostly stable after 2 h but with the majority of material having crashed out after 24 h.

It was also noted in a control experiment that swelling and shrinking of the superhydrophobic Sylgard-184 films in the solvent under the same conditions as the encapsulation, but without any nanoparticle dispersion, brought about no change in the contact angle or wetting behavior of the films, demonstrating that this technique is non-destructive towards the films, and therefore that any changes to these properties would be conferred by the nanoparticles themselves.

### 3.3. Functionalising tungsten (VI) oxide nanoparticles

As-purchased tungsten (VI) oxide nanopowder (< 100 nm) was functionalised by esterification of surface tungstenol

groups (W-OH) with fatty oleate chains as per the literature general method [6]. The reaction appeared successful given that while unfunctionalised  $\text{WO}_3$  nanoparticles could not be dispersed at all in most organic solvents, the functionalized material formed a good, milky-yellow dispersion in chloroform. Fourier-Transform Infra-Red (FTIR) analysis of the resulting yellow powder confirmed the shift of the C=O stretch band from 1709 to 1741  $\text{cm}^{-1}$  between pure oleic acid and the oleate-functionalised nanoparticles (Figure 4). Other hydrocarbon bands also appeared in the  $\text{WO}_3$ -oleate spectrum at 2950 (C-H stretch), 1400 and 1220  $\text{cm}^{-1}$  (C-H bends), while weaker bands could also be seen for  $\text{WO}_3$  at 1453 and 1142  $\text{cm}^{-1}$ , corresponding to W-O-H and W-OH bending modes respectively [15,16].

### 3.4. Characterization of the films

Superhydrophobic polymer films swell-encapsulated with oleic acid-functionalised tungsten (VI) oxide nanoparticles in chloroform for 2 h were white in colour and passed the scotch tape test both before and after the nanoparticle incorporation. All superhydrophobic films synthesised exhibited Cassie-Baxter [17] wetting, in which a roughly spherical water droplet would easily roll about the surface of the film. This was similar to the untreated superhydrophobic polymer film, however with slightly reduced contact angles correlating with increased  $\text{WO}_3$  loading (Figure 5).

Furthermore, a droplet bouncing experiment demonstrated that a droplet of an aqueous solution of methylene blue

would bounce twice off of the surface of the WO<sub>3</sub>-oleate/polymer film (Figure 6); the same number was also observed for the untreated superhydrophobic film.

SEM imaging revealed that the developed microstructure of the material remained mostly unchanged by the swelling process, with most surface features on the scale of approxi-

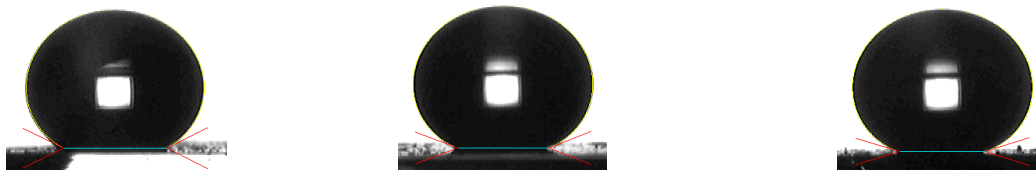


**Figure 5.** 5 µL water droplets on superhydrophobic Sylgard-184 films, swell-encapsulated with WO<sub>3</sub>-oleate nanoparticle dispersion in chloroform for 2 h at relative concentrations of 100% (saturated dispersion, left), 25% (centre) and 0% (pure chloroform, right), with mean contact angles of  $\theta = 151, 157$  and  $161^\circ$  respectively and a standard deviation of  $2^\circ$ , using Laplace-Young droplet fitting.

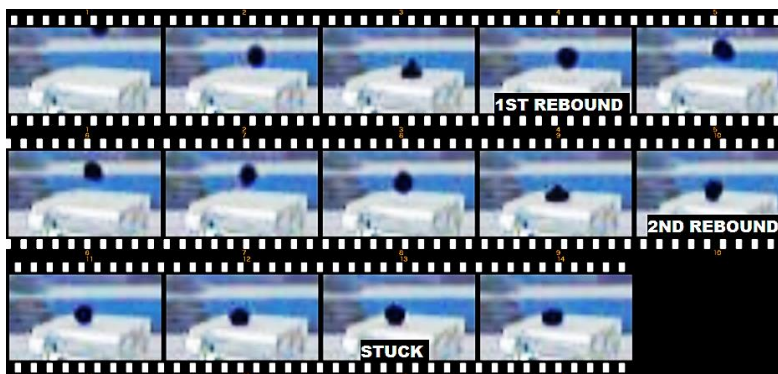


**Figure 6.** Droplet of aqueous methylene blue of arbitrary volume, dropped from arbitrary height, bounces twice before becoming stuck on the superhydrophobic Sylgard-184 film swell-encapsulated with a saturated chloroform dispersion of WO<sub>3</sub>-oleate nanoparticles. The same was observed for the pure polymer film.

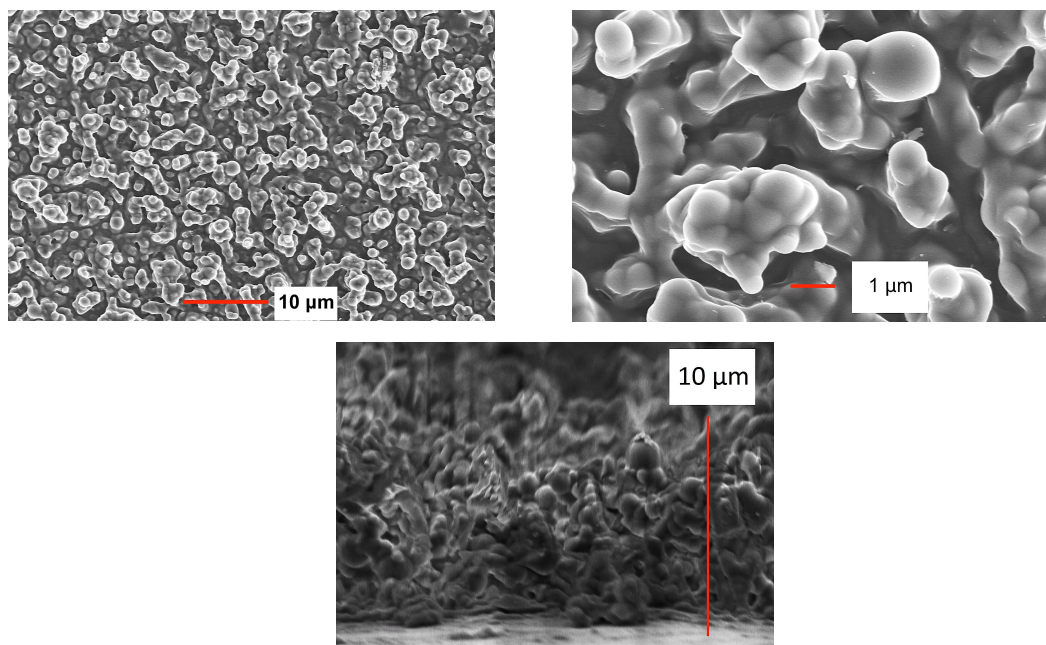
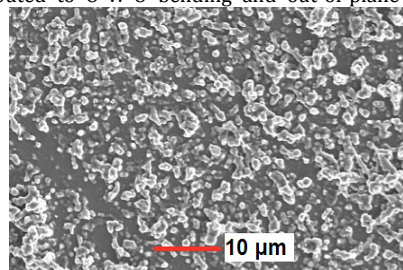


**Figure 7.** Top-down (upper) and side-on (lower) SEM images of pure polymer superhydrophobic film at magnifications 2,000 $\times$  (upper-left), 10,000 $\times$  (upper-right) and 4,000 $\times$  (lower centre).

mately 0.5 - 2.0 µm (Figure 7 and 8). Surface features retained their globular morphology, suggesting that much of the nanoparticle material had been encapsulated deep within the polymer.

The Raman spectrum was measured for the film obtained from the dilute WO<sub>3</sub>-oleate dispersion, and is shown in Figure 9. The bands at 807, 716 and 274 cm<sup>-1</sup> represent O-W-O stretching, W-O stretching and dangling O-W-O bending modes respectively, and are characteristic and typical of monoclinic

WO<sub>3</sub>. The blue shift of the O-W-O bending mode of dangling oxygen at 274 cm<sup>-1</sup>, observed at 271 cm<sup>-1</sup> in the literature [18], may be an effect of the functionalization of surface W-OH groups with the oleate groups. The bands at 328 and 239 cm<sup>-1</sup> are attributed to O-W-O bending and out-of-plane wagging



modes respectively within the lattice. Meanwhile, the weak band at 613 cm<sup>-1</sup> has been ascribed to the lattice vibration of hydrated WO<sub>3</sub>(H<sub>2</sub>O)<sub>x</sub> [19].

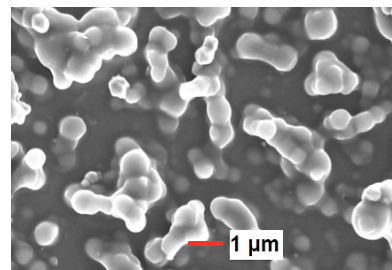


Figure 8. SEM images at 2,000× (left) and 10,000× (right) magnification of superhydrophobic WO<sub>3</sub> nanocomposite film.

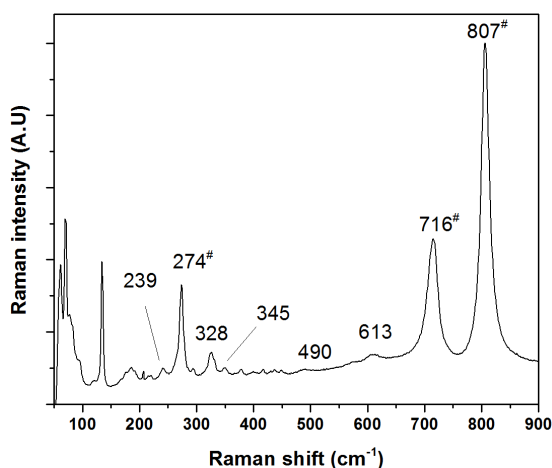


Figure 9. Raman spectrum of superhydrophobic WO<sub>3</sub> nanocomposite film from dilute dispersion. Peaks labelled with a (#) sign correspond to monoclinic WO<sub>3</sub>.

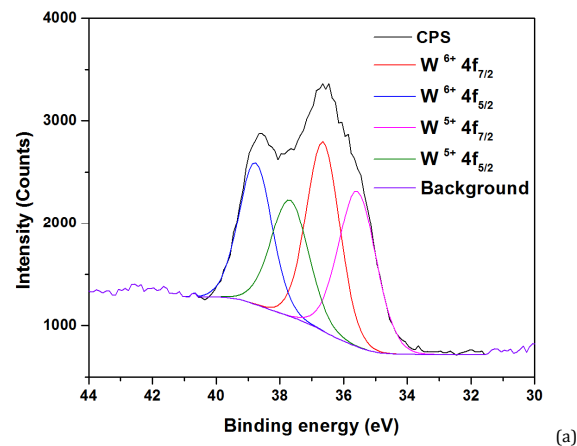
Other sharp but weak Raman bands appearing between 200 and 650 cm<sup>-1</sup> have previously been ascribed to modes in the substoichiometric WO<sub>3-x</sub> [20]. Bands below 235 cm<sup>-1</sup> in wavenumber can be assigned as low-frequency temperature-dependent phonons in the material [21]. The nanoscale size of the WO<sub>3</sub> means bands usually observed in the bulk at 490 and 519 cm<sup>-1</sup>, both typically attributed to the O lattice vibrational mode [18], are absent. Rather, the broad artefact at 490 cm<sup>-1</sup> is more likely attributed to Si-O-Si symmetric stretching in the polydimethylsiloxane matrix [22]. Other peaks arising from the polymer, usually appearing at 687, 708 and 787 cm<sup>-1</sup> for Si-CH<sub>3</sub> symmetric rocking, Si-C symmetric and asymmetric stretching respectively appear to have been absorbed by the dominant broad WO<sub>3</sub> peaks at 716 and 807 cm<sup>-1</sup> [22].

Energy-dispersive X-ray (EDX) elemental analysis confirmed the presence of 4.5 at % W in the saturated sample with respect to carbon, with 2.0 at % W for the sample obtained from the dilute WO<sub>3</sub>-oleate dispersion.

X-ray photoelectron spectroscopy area scans of the films revealed broadening of the peaks between 34 and 40 eV, as shown in Figure 10. These were deconvoluted into two spin-orbit coupling doublets, similar in area - the first doublet, corresponding to the binding energies of 4f<sub>7/2</sub> and 4f<sub>5/2</sub> electrons respectively for W<sup>6+</sup>, appeared at 36.7 and 38.8 eV. The second doublet at lower energy corresponds to W<sup>5+</sup>, with binding energies at 35.8 and 38.0 eV for 4f<sub>7/2</sub> and 4f<sub>5/2</sub> electrons respectively [23]. These results were consistent with the expectation of W<sup>5+</sup> in tungsten bronzes H<sub>x</sub>WO<sub>3</sub> (which

gives rise to the photochromic effect). The doublet observed in the lower-concentration spectrum appears at 36.5 and 38.4 eV, which corresponds to an overlapping of W<sup>6+</sup> and W<sup>5+</sup> 4f<sub>7/2</sub> and 4f<sub>5/2</sub> binding energies, which at this intensity was difficult to deconvolute.

The XPS peak areas reflected the expected pattern in the concentrations of W in the films, with good agreement between survey- and narrow-scans for the saturated loaded sample of 0.78 ± 0.12 at % with respect to carbon. W for the 25% loading sample could not be quantified from the survey scan, but narrow scan analysis suggested 0.03 ± 0.02 at %. This seems an unlikely figure in light of the figures from both the saturated film and the EDX scans, so perhaps the W present at the surface of the film is below the XPS limit of quantification for the dilute sample.



(a)

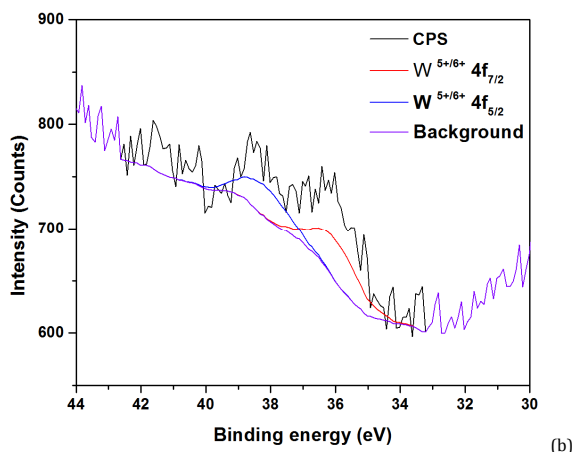


**Figure 10.** X-ray photoelectron spectra of superhydrophobic polymer films swell-encapsulated with  $\text{WO}_3$ -oleate dispersion at 100% (a) and 25% (b) saturation. The lower-energy doublet in the upper spectrum corresponds to partially reduced  $\text{W}^{5+}$ , while the higher-energy doublet represents the more abundant  $\text{W}^{6+}$ .  $\text{W}^{6+/5+}$  could not be resolved in the lower spectrum.

The discrepancy between the XPS and EDX elemental analyses is to be expected; whilst both will scan areas of similar lateral dimensions (approx. 1000 nm), the XPS technique is highly surface-sensitive, only detecting elements up to a depth of approximately 10 nm beneath the film surface. On the other hand, EDX scans much deeper, detecting elements at depths on the order of around 1000 nm or more beneath the surface. Therefore, the fact that the EDX is detecting so much more W than the XPS is indicative that the nanoparticles have thoroughly penetrated the polymer film, whilst the XPS also indicates that a significant amount of material is available at the surface of the polymer. This is an important consideration for nanoparticles such as these, whose photochromism and photocatalysis are so dependent on having an exposed surface.

The XPS data suggest a high relative abundance of  $\text{W}^{5+}$  with respect to  $\text{W}^{6+}$  - while of course the latter is most abundant in  $\text{WO}_3$ , the reduced form appears to come close. Peak area analysis reveals that the ratio of  $\text{W}^{6+}:\text{W}^{5+}$  in the saturated sample is just  $1.06 \pm 0.33$ . A thoroughly reduced tungsten bronze  $\text{H}_x\text{WO}_3$  (with a high value of  $x$ ) will exhibit a blue colour; [24] however, the nanoparticles here are yellow. The apparent abundance of  $\text{W}^{5+}$  here is again indicative of the surface sensitivity of XPS. Given that partial reduction of  $\text{W}^{6+}$  to  $\text{W}^{5+}$  tends to occur at the surface of the nanoparticle by way of proton and oxygen exchange with the surrounding medium [12,25], this observation is consistent with the high specific surface area of the  $\text{WO}_3$  nanoparticles, in which surface composition is the dominating factor over bulk.

The X-ray diffraction (XRD) for the  $\text{WO}_3$ -encapsulated Sylgard-184 films appear somewhat as expected (Figure 11); while features at higher  $2\theta$  values were difficult to resolve, all patterns observed feature the three peaks at  $2\theta = 23.1$ ,  $23.6$  and  $24.4^\circ$  characteristic of monoclinic  $\text{WO}_3$  [24]. These are in strong agreement with the powder XRD pattern for the standalone  $\text{WO}_3$  nanopowder. It is also possible to see some amorphous structure in the nanocomposites, featuring broad peaks over the ranges  $2\theta = 15$ - $32^\circ$  and  $32$ - $35^\circ$ . This may arise from the partial reduction of  $\text{WO}_3$  by the swelling process, which leads to random local charge imbalances which distort the  $\text{WO}_6$  octahedra that comprise the  $\text{WO}_3$  lattice. The result is a material whose crystal planes have become warped, leading to a loss of crystal structure, but whilst retaining good short-range order. As such, broad peaks in the XRD diffraction pattern may have been observed on account of the partially reduced, amorphous, nonstoichiometric  $\text{H}_x\text{WO}_3$  [23,26]. This is

supported by the XPS data, which indicates the presence of both  $\text{W}^{6+}$  and  $\text{W}^{5+}$  environments, the Raman, which identifies W-O stretching modes for amorphous material, and possibly also the FT-IR, which features non-terminal W-OH and WO-H bending modes.

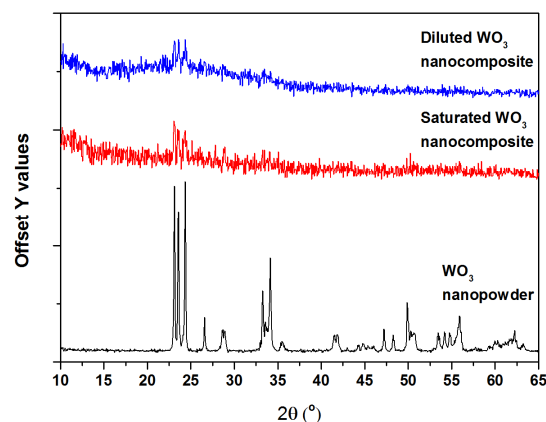


**Figure 11.** XRD patterns for superhydrophobic polymer films swell-encapsulated with  $\text{WO}_3$ -oleate nanoparticle dispersions at 25% and 100% saturation, and for as-purchased  $\text{WO}_3$  nanopowder.

#### 4. Conclusions

It has been demonstrated that superhydrophobic  $\text{WO}_3$ /polymer nanocomposite thin films can be produced from a tandem AACVD-swell-encapsulation procedure. Limitations in preliminary attempts at nanoparticle incorporation by a one-pot AACVD technique were demonstrated, then overcome by the present method. The sequence presented here confers far greater control over the properties of both components of the composite material than alternative nanoparticle incorporation methods. It has been demonstrated that control over the quantity of nanoparticle material incorporated within the polymer film is a trivial matter of simply adjusting the concentration of the swelling medium, as supported by elemental analysis. These analyses also demonstrate that tungsten (VI) oxide nanoparticles exist both deeply embedded within the polymer matrix and close to the surface for such surface-dependent properties as photochromism and photocatalysis, which may be practically demonstrated in future work. This work will set the foundation for future studies investigating the functional properties of these films.

#### References

- Cheng, Y. T.; Rodak, D. E. *Appl. Phys. Lett.* **2005**, *86*(14), 144101.
- Barthlott, W.; Neinhuis, C. *Planta* **1997**, *202*(1), 1-8.
- Marchand, P.; Hassan, I. A.; Parkin, I. P.; Carmalt, C. J. *Dalton Trans.* **2013**, *42*(26), 9406-9422.
- Wang, Z.; Su, Y.; Li, Q.; Liu, Y.; She, Z.; Chen, F.; Li, L.; Zhang, X.; Zhang, P. *Mater. Charact.* **2015**, *99*, 200-209.
- Crick, C. R.; Parkin, I. P. *Thin Solid Films* **2010**, *518*(15), 4328-4335.
- Crick, C. R.; Bear, J. C.; Southern, P.; Parkin, I. P. *J. Mater. Chem. A* **2013**, *1*(13), 4336-4344.
- Wong, B.; Yoda, S.; Howdle, S. M. *J. Supercrit. Fluids* **2007**, *42*(2), 282-287.
- Yang, Z.; Dasog, M.; Dobbie, A. R.; Lockwood, R.; Zhi, Y.; Meldrum, A.; Veinot, J. G. C. *Adv. Funct. Mater.* **2014**, *24*(10), 1345-1353.
- Perni, S.; Piccirillo, C.; Pratten, J.; Prokopovich, P.; Chrzanowski, W.; Parkin, I. P.; Wilson, M. *Biomaterials* **2009**, *30*(1), 89-93.
- Azuma, C.; Kawano, T.; Kakemoto, H.; Irie, H. *J. Appl. Phys.* **2014**, *116*(17), 173502.
- Gavrilyuk, A. *Electrochim. Acta* **1999**, *44*(18), 3027-3037.
- Wang, S.; Kershaw, S. V.; Li, G.; Leung, M. K. H. *J. Mater. Chem. C* **2015**, *3*(14), 3280-3285.
- Ramana, C. V.; Utsunomiya, S.; Ewing, R. C.; Julien, C. M.; Becker, U. *J. Phys. Chem. B* **2006**, *110*(21), 10430-10435.

- [14]. Lee, J. N.; Park, C.; Whitesides, G. M. *Anal. Chem.* **2003**, *75*(23), 6544-6554.
- [15]. Rougier, A.; Portemer, F.; Quede, A.; El Marssi, M. *Appl. Surf. Sci.* **1999**, *153*(1), 1-9.
- [16]. Badilescu, S. *Solid State Ion* **2003**, *158*(1-2), 187-197.
- [17]. Cassie, A. B. D.; Baxter, S. *Nature* **1945**, *155*(3923), 21-22.
- [18]. Garcia-Sanchez, R. F.; Ahmido, T.; Casimir, D.; Baliga, S.; Misra, P. J. *Phys. Chem. A* **2013**, *117*(50), 13825-13831.
- [19]. Daniel, M. F.; Desbat, B.; Lassegues, J. C.; Gerand, B.; Figlarz, M. J. *Solid State Chem.* **1987**, *67*(2), 235-247.
- [20]. Frey, G. L.; Rothschild, A.; Sloan, J.; Rosentsveig, R.; Popovitz-Biro, R.; Tenne, R. J. *Solid State Chem.* **2001**, *162*(2), 300-314.
- [21]. Salje, E.; Viswanathan, K. *Acta Crystallogr. Sect. A* **1975**, *31*(3), 356-359.
- [22]. Bae, S. C.; Lee, H.; Lin, Z.; Granick, S. *Langmuir* **2005**, *21*(13), 5685-5688.
- [23]. Gogova, D.; Gesheva, K. *Phys. Stat. Sol. A* **1999**, *176*, 969-984.
- [24]. Ashraf, S.; Blackman, C. S.; Palgrave, R. G.; Parkin, I. P. J. *Mater. Chem.* **2007**, *17*(11), 1063-1070.
- [25]. He, T.; Yao, J. J. *Mater. Chem.* **2007**, *17*(43), 4547-4757.
- [26]. Li, C.; Hsieh, J. H.; Hung, M. T.; Huang, B. Q. *Vacuum* **2015**, *118*, 125-132.